Evaluation of Characterization Techniques for Iron Pipe Corrosion Products and Iron Oxide Thin Films

Thomas Borch[1]; Anne K. Camper[2]; Joel A. Biederman[3]; Phillip W. Butterfield[4]; Robin Gerlach[5]; and James E. Amonette[6]

Abstract: A common problem faced by drinking water studies is that of properly characterizing the corrosion products (CP) in iron pipes or synthetic Fe (hydr)oxides used to simulate the iron pipe used in municipal drinking-water systems. The present work compares the relative applicability of a suite of imaging and analytical techniques for the characterization of CPs and synthetic Fe oxide thin films and provide an overview of the type of data that each instrument can provide as well as their limitations to help researchers and consultants choose the best technique for a given task. Crushed CP from a water distribution system and synthetic Fe oxide thin films formed on glass surfaces were chosen as test samples for this evaluation. The CP and synthetic Fe oxide thin films were analyzed by atomic force microscopy (AFM), scanning electron microscopy (SEM), energy-dispersive spectroscopy, time-of-flight secondary ion mass spectrometry (ToF-SIMS), X-ray powder diffractometry (XRD), grazing incident diffractometry (GID), transmission electron microscopy (TEM), selected area electron diffraction, X-ray photoelectron spectroscopy (XPS), Fourier transform infrared, Mössbauer spectroscopy, Brunauer–Emmett–Teller N_2 adsorption and Fe concentration was determined by the ferrozine method. XRD and GID were found to be the most suitable techniques for identification of the mineralogical composition of CP and synthetic Fe oxide thin films, respectively. AFM and a combined ToF-SIMS–AFM approach proved excellent for roughness and depth profiling analysis of synthetic Fe oxide thin films, respectively. Corrosion products were difficult to study by AFM due to their surface roughness, while synthetic Fe oxide thin films resisted most spectroscopic methods due to their limited thickness (118 nm). XPS analysis is not recommended for mixtures of Fe (hydr)oxides due to their spectral similarities. SEM and TEM provided great detail on mineralogical morphology.

DOI: 10.1061/(ASCE)0733-9372(2008)134:10(835)

CE Database subject headings: Water distribution systems; Corrosion; Iron; Spectral analysis; Microscopy; Disinfection; Biofilm; Organic matter.

Introduction

As stated in a recent National Research Council report (NRC 2006), "The distribution system is the remaining component of public water supplies yet to be adequately addressed in national efforts to eradicate waterborne disease." One component of an overall strategy to improve the function of distribution systems is to protect water quality by limiting transformations that occur due to interactions with pipe surfaces, which includes biofilm growth, leaching internal corrosion scale formation, nitrification, and other chemical reactions. A critical component of these issues is pipe material, and iron pipes are a major consideration because of their reactivity. In the United States approximately 15% of all pipelines supplying drinking water are unlined cast iron pipes (AWWA 2003). Corrosion products (CP) easily form at the iron-water interface and can lead to undesirable changes in the drinking water quality within the distribution system (Sarin et al. 2004). CP react with chlorine based disinfectants resulting in a reduction of disinfectant residual (Kazi et al. 2006; Sarin et al. 2001). The presence of unlined cast iron pipe has been correlated with an increase in total coliforms (LeChevallier et al. 1996), which are indicators of possible fecal contamination. It has been shown that biofilms forming on the walls of pipelines can contain a number of undesirable organisms, and that biofilms form more readily when CP and natural organic mater (NOM) are present (Butterfield et al. 2002). The adsorption of NOM to CP is believed to promote biofilm growth. Therefore, it has been recognized that in order to understand the complex interactions among CP, biofilms, NOM, and other water constituents, it is vital to characterize the minerals that comprise the CP (Sarin et al. 2001; Vikesland and Valentine 2002).

Synthetic iron (hydr)oxides or CP analogs are often used to simulate CP in drinking water distribution systems for improved homogeneity in experimental systems (Butterfield et al. 2002; Szabo et al. 2007; Vikesland and Valentine 2002; Williams and

[1]Assistant Professor, Dept. of Soil and Crop Sciences and Dept. of Chemistry, Colorado State Univ., Fort Collins, CO 80523-1170 (corresponding author). E-mail: borch@colostate.edu

[2]Professor, Dept. of Civil Engineering and Center for Biofilm Engineering, Montana State Univ., 366 EPS Building, Bozeman, MT 59717. E-mail: anne_c@biofilm.montana.edu

[3]Instructor, Suffield Academy, 185 North Main St., Suffield, CT 06078.

[4]Associate Research Professor, Dept. of Civil and Environmental Engineering, Washington State Univ., Health Sciences Building 325 M, P.O. Box 1495, Spokane, WA 99210-1495.

[5]Associate Professor, Dept. of Chemical and Biological Engineering and Center for Biofilm Engineering, Montana State Univ., Bozeman, MT 59717.

[6]Senior Research Scientist, Pacific Northwest National Laboratory, P.O. Box 999, K8-96, Richland, WA 99352.

Note. Discussion open until March 1, 2009. Separate discussions must be submitted for individual papers. The manuscript for this paper was submitted for review and possible publication on December 4, 2007; approved on February 27, 2008. This paper is part of the ***Journal of Environmental Engineering***, Vol. 134, No. 10, October 1, 2008. ©ASCE, ISSN 0733-9372/2008/10-835–844/$25.00.

Braun-Howland 2003), however, potential problems can arise from oversimplification of natural iron (hydr)oxide mixtures being modeled as demonstrated previously (Perret et al. 2000). In addition, application of synthetic iron (hydr)oxides to granular filter media has been used for the removal of particulates and organic matter and for the immobilization of metals (e.g., arsenic) and radionuclides (e.g., strontium) from waste-, drinking-, and groundwater (Benjamin et al. 1996; Chang et al.1997; Cheng et al. 2004; Hansen et al. 2001; Joshi and Chaudhuri 1996; Korshin et al. 1997; Lai and Chen 2001; Solozhenkin et al. 2007; Stenkamp and Benjamin 1994; Thirunavukkarasu et al. 2001).

CP are composed primarily of iron (hydr)oxides (Sarin et al. 2001). The different metal (hydr)oxide phases comprising CP possess different chemical properties such as free energy of formation, crystal structure, morphology, and sorptive properties. The highly reactive nature of iron (hydr)oxides often results in the formation of surface layers with properties distinctly different from the bulk. Thus to determine the relative impact or reactivity of the different iron (hydr)oxides present in drinking water distribution systems one must often rely on systematic investigations of well-characterized synthetic iron (hydr)oxides to better understand how iron (hydr)oxides control biofilm, humic acids (HA), and disinfection (by)product interactions with CP (Appenzeller et al. 2002; Butterfield et al. 2002; Chun et al. 2005, 2007; Vikesland and Valentine 2002).

Characterization of corrosion products is, however, not a straightforward task due to the wide range of instruments capable of analyzing iron and the complexity of data interpretation. Consequently, the objectives of this work were to: (1) evaluate a variety of bulk and surface analytical techniques for the characterization of crushed tubercles (McNeill and Edwards 2001) from the interior of a corroded drinking water pipe and a synthetic iron (hydr)oxide thin film; and (2) provide an overview of the type of results that commonly available bench-top instruments can provide, including some of their major limitations. It was beyond the scope of this work to include synchrotron radiation based instruments for the characterization of iron (hydr)oxides due to their complexity and limited access (Borch et al. 2007; O'Day et al. 2004; Parsons et al. 2002). The results described here can assist in interpreting the response of engineered and experimental systems where internal corrosion produces iron oxide phases that interact with disinfectants and NOM, and often support biofilm growth.

Materials and Methods

Iron (Hydr)Oxides

The CP and synthetic iron oxide investigated were the same as those used in a water distribution study described previously (Butterfield et al. 2002). The crushed CP were from an unlined cast iron pipe, while the synthetic iron oxide was deposited as a thin film on a glass substratum. CP were obtained from an iron pipe recovered from a water distribution system in the greater Boston area (United States) that had been in operation for approximately 80 years. CP were dried under a flow of N_2 and crushed. Particles analyzed passed a No. 10 (2.00 mm) sieve. CP were subsequently washed using oxygen-free Nanopure (Barnstead-Thermolyne, Dubuque, Iowa) reagent-grade water, dried, and stored under N_2. During the removal, crushing, and sieving processes the CP were exposed to atmospheric oxygen and some oxidation may have occurred. However, the aim was not to characterize the CP in its pure natural state as attempted previously by Sarin et al. (2001), but rather to compare analytical techniques for characterization of CP and iron (hydr)oxide thin films to help researchers and consultants choose the best analytical approach. Glass beads (GB) with a nominal diameter of 0.5 mm (Biospec Products, Inc., Bartlesville, Okla.) were coated with iron oxides [iron oxide coated glass beads (IOCB)] using a forced acid hydrolysis technique similar to the protocols of Rieke et al. (1995) with exception of the sulfonated self-assembled monolayer. IOCB were rinsed with Nanopure water, dried at room temperature, and stored under N_2. The same iron oxide coating technique was applied to glass coverslips [iron oxide coated coverslip (IOCC)] (Fisher Scientific, 0.13–0.17 mm thickness). IOCC were analyzed by atomic force microscopy (AFM), Mössbauer spectroscopy, Fourier transform infrared (FTIR) and grazing incidence diffraction (GID) to avoid geometric constraints of spherical IOCB. Iron oxides could alternatively be removed from the glass surface using mild sonication followed by FTIR and Mössbauer spectroscopy analysis as described previously (Borch et al. 2007).

Five iron oxides in powder form were used as reference compounds in this investigation: hematite (α-Fe_2O_3), goethite (α-FeOOH) magnetite (Fe_3O_4) and maghemite (γ-Fe_2O_3), all commercial products (Alfa Aesar, Ward Hill, Mass.), and two-line ferrihydrite ($Fe_{1.55}O_{1.66}(OH)_{1.33}$) synthesized according to Cornell and Schwertmann (1996).

Bulk Properties

The total iron content of the CP and IOCB was determined (Hach Method 8147-FerroZine Method) by digestion in concentrated HCl and subsequent spectrophotometric analysis (Butterfield et al. 2002). The specific surface area of GB, IOCB, and CP samples was measured with a FlowSorb 2300 (Micromeritics, Norcross, Ga.) using a three-point Brunauer, Emmett, and Teller (BET) N_2 sorption isotherm.

Scanning Electron Microscopy and Energy Dispersive Spectroscopy

Scanning electron microscopy (SEM) and energy dispersive spectroscopy (EDS) were applied to obtain high resolution images and the elemental composition. The instrument used was a JEOL 6100 SEM with a LaB_6 source (JEOL USA Inc., Peabody, Mass.) coupled to a Noran Voyager X-ray detector for elemental analysis (1 μm spot size, Thermo NORAN Inc., Middleton, Wis.), and a Rontec Xflash detector for elemental mapping (Rontec USA, Inc., Acton, Mass.). EDS spectra in the range of 0–10 eV were obtained using an accelerating voltage of 15 kV. The working distance was 8–39 mm for high-resolution imaging and 39 mm for EDS analysis and elemental mapping. All samples were carbon coated before SEM and EDS analysis. Digital imaging (using both secondary electron and backscattered electron signals), EDS spot analysis, and two-dimensional elemental mapping were used to distinguish mineral phases and characterize their morphology, texture, and composition.

AFM

AFM was used to obtain three-dimensional (3D) topographic images. Image analysis provided roughness and surface area information with subnanometer height resolution under both wet and dry conditions. IOCB and GB were carefully pressed into soft indium foil before they were mounted to the sample stage. CP

proved too rough for our instrument. IOCC samples were mounted with double-sided tape to the sample disk, and an uncoated glass cover slip (UC) was used as a reference. All AFM images were obtained using a Nanoscope IIIa Extended Multimode AFM from Veeco Metrology (Santa Barbara, Calif.). Tapping mode images in air were obtained using silicon tips and cantilevers (TAP 300 HD with a nominal tip radius of less than 10 nm and a specified nominal cantilever spring constant of 40 N/m from Nano-Devices, Santa Barabara, Calif.). Contact mode images, in both air and liquid, were obtained using silicon nitride tips and cantilevers [TM microscopes (NPS 20) with a specified nominal cantilever spring constant of 0.3 N/m]. Height images were minimally processed using a first-order flatten procedure to prevent introduction of artifacts (Instruments 1997).

Depth Profiling by Time-of-Flight Secondary Ion Mass Spectrometry/AFM

Time-of-flight secondary ion mass spectrometry (ToF-SIMS) was used to recover fragments of ionized molecules from the outermost atomic layer of the surface. ToF-SIMS/AFM for depth profiling has the advantage of sample imaging, spatial resolution, and high surface sensitivity (Arce et al. 2003). The IOCC coating was depth profiled using a TRIFT I ToF-SIMS (PHI-Evans, Eden Prairie, Minn.) with a pulsed gallium liquid metal ion gun fired at 25 keV with a 10-kHz repetition rate, serving as the primary ion source. IOCC and UC samples were sputter coated with gold (less than 10 nm) to prevent charge buildup and then introduced into a vacuum of less than 1×10^{-8} torr. The raster area for sputtering was 40 μm^2, while the raster area for analysis of secondary ions was 25 μm^2 in the center of the sputtered area. Sputtering intervals for depth profiling were 15 s, and secondary ion collection intervals were 60 s. The boundary between the glass and the iron oxide coating of IOCC was located by sputtering the surface and monitoring iron and silicon peaks until the counts for silicon ceased to increase with further sputtering. The depth of the ablation pits was directly measured using the section analysis mode of the AFM.

Transmission Electron Microscopy and Selected Area Electron Diffractometry

Transmission electron microscopy (TEM)-selected area electronic diffractometry (SAED) was applied to obtain atomic-resolution images and crystal information on selected areas. Specimens of the synthetic coating were prepared by sonication of IOCB in de-ionized water and collection of the suspended material onto a C-coated Cu grid with a formvar support film. CP were deposited directly onto the Cu grid. Imaging and analyses were performed using a JEOL 2010 high resolution TEM (JEOL USA Inc., Peabody, Mass.), equipped with a LaB_6 filament, and operated at 200 kV with a resolution of 1.9 Å. The JEOL 2010 was coupled to a Oxford EDS system using Link ISIS analytical software. Images were analyzed using Digital Micrograph software (Gatan Inc., Pleasanton, Calif.). SAED ring patterns formed by nanoparticles were collected and evaluated by Desktop Microscopist software (Lacuna Laboratories, Tempe, Ariz.). The nominal accuracy of the d spacings was approximately 0.1 Å.

Mössbauer Spectroscopy

Mössbauer spectroscopy was applied to obtain information about the type and potential distribution of amorphous and/or crystalline Fe (hydr)oxide(s) on the IOCC. Mössbauer spectroscopy is used extensively in the study of corrosion and is especially powerful for the identification and quantification of nanophase iron oxides (Cook 2004; Vertes and Czakonagy 1989). IOCC samples were analyzed at room temperature by conventional transmission Mössbauer spectroscopy using a 50 mCi Co-57 single-line thin source mounted on Rh foil and a WissELL MVT-1000 velocity transducer. For more details please refer to Kukkadapu et al. (2004).

FTIR

FTIR was applied to the IOCC to obtain information about the nature of the Fe thin film. The IOCC was analyzed by infrared transmission, internal reflectance, and specular reflectance spectroscopy using an UC for the background. A Bruker IFS66V/S spectrometer equipped with a KBr beamsplitter and deuterated triglycine sulfate (DTGS) detector and specular reflectance accessory was used to collect the reflectance spectra, which were converted to absorbance using the Kramers–Kronig transformation. Each spectrum was the sum of 128 scans collected at 4 cm^{-1} resolution and apodized using the Blackman–Harris three-term function.

X-Ray Photoelectron Spectroscopy

X-ray photoelectron spectroscopy (XPS) was applied to achieve information of binding energies, elemental composition, and oxidation states. IOCC, UC samples, and the reference compounds were analyzed directly. The CP were ground to a powder with a Diamonite (sapphire) mortar and pestle and inserted rapidly ($<$5 min) under ambient conditions. Spectra were collected with a Model 5600ci spectrometer (Perkin Elmer Corp.) employing a monochromated Al $K\alpha$ X-ray source (1486.6 eV) at 300 W and a 5 eV flood gun. Pass energies of 58.7 eV were used for broad scans and 5.85 (IOCC/UC) and 23.5 (CP) eV for high resolution scans. Binding energies were referenced to the adventitious carbon peak (C 1s) at 285.0 eV. Component positions were determined by the location of individual Gaussian–Lorentzian peaks, obtained by deconvolution of the XPS spectra using a nonlinear least-squares fitting routine with adjustable polynomial baseline using RBD AugerScan 3.0.1 software.

Powder and Grazing Incidence (GI) X-Ray Diffractometry

X-ray diffractometry (XRD) was applied for bulk characterization of crystalline materials. The X-ray diffraction apparatus used in this study was a Philips X Pert MPD system. The X-ray source was operated at 40 kV, 50 mA (LAMBD=Cu $K\alpha 1$, 1.5406 Å). Wavelength selection was achieved with a graphite diffracted beam monochromator, and the detector was a Xe-filled proportional counter. The specimen holder was a single-crystal quartz plate. The diffractometer was controlled using the Philips X Pert software suite (X Pert Data Collector, V1.3d). Data analysis was accomplished using Jade V6.5.7 (Materials Data, Inc., Livermore, Calif.) and the powder diffraction file database (PDF-2, 2002 release, international centre for diffraction data, Newtown Square, Pa.). The CP were ground to a powder with a Diamonite mortar and pestle. Scan parameters were: $2\theta = 5.00 - 75.00^{\circ}$, and the scan rate was $0.02^{\circ}/5$ s. The iron oxide thin film was examined in grazing-incidence geometry on a 220-mm 2θ goniometer radius. The incident-beam optic was a Göbel mirror (parallel beam). The

receiving optics were a 0.27 rad parallel plate collimator and a flat graphite monochromator. The incident-beam angle (OMEGA) was fixed at 2.50°, and the scan axis was 2θ. The scan range was 15.00–75.00°, and the scan rate was 0.05°/45 s. The beam spot was approximately 20 mm wide and, at OMEGA=2.50°, approximately 27 mm long.

Results and Discussion

Bulk Properties

The iron concentration and the BET surface area (SA) of CP and IOCB were determined to estimate the maximum amount of Fe available for surface reactions. The iron content of the IOCB was 7.35 mg Fe (coating)/m^2 beads. This result is similar to that reported for sand coated by baking with $FeCl_3$ sludges (9.33 mg/m^2) (Korshin et al. 1997) and three times lower than that reported for the adsorption of goethite crystals to sand (24.2 mg/m^2) (Scheidegger et al. 1993). Iron content of the CP was 22.4 mg Fe/m^2 CP, approximately three times greater than that of the IOCB. Reactive surface areas for IOCB and GB were 0.068 ± 0.01 and 0.064 ± 0.02 m^2/g, respectively, based on BET analysis. On a per gram basis, BET areas for IOCB are 40 times lower than those reported for sand coated by baking with $FeCl_3$ sludges (Korshin et al. 1997). The measured surface area of 26.2 ± 0.69 m^2/g for CP fell within the range of values reported from various studies of natural and synthetic iron (hydr)oxide crystals (Cornell and Schwertmann 1996) and comparable to a reported surface area (21.3 m^2/g) of goethite (Scheidegger et al. 1993), which was later observed to be the major iron phase in CP. These results were just below the range of 32–82 m^2/g reported for corrosion scales from old iron drinking water pipes in the Boston area (Sarin et al. 2001). The higher surface area observed by Sarin et al. (2001) might be due to the pulverization process during sample preparation; this study selected particles of a certain sieve size. The importance of these results was evident in our previous experiments where CP showed higher reactivity than IOCB toward both humic substances and disinfectants (Butterfield et al. 2002).

SEM and EDS

Representative SEM images are shown in Fig. 1. Comparison of the GB image [Fig. 1(a)] with the IOCB image [Fig. 1(b)] shows limited impact of the coating on the overall physical structure of the surface (due to the inherent roughness of the GB), which is consistent with the BET results. For CP, most images could be divided into four distinct morphological types [Figs. 1(c–f)], which were similar to those found in other published SEM images of corroded iron pipes (Smith et al. 1996).

Visual identification of the morphologies present in the CP proved challenging, however the crystals observed in Fig. 1(c) appear like multidomainic or bipyramidal crystals (e.g., goethite) or the structures could alternatively be octahedral crystals (e.g., magnetite) (Cornell and Schwertmann 1996). The hexagonal structures in Fig. 1(d) appear to be green rust covered with needle shaped goethite (Cornell and Schwertmann 1996; Peulon et al. 2003; Refait et al. 2003). The globular structures in Fig. 1(e) are likely magnetite (Cornell and Schwertmann 1996; Dong et al. 2000); interestingly, cocci-shaped bacteria were found inside some of these globules (data not shown) similar to studies by Dong et al. (2000). Fig. 1(f) seems to represent microcrystalline

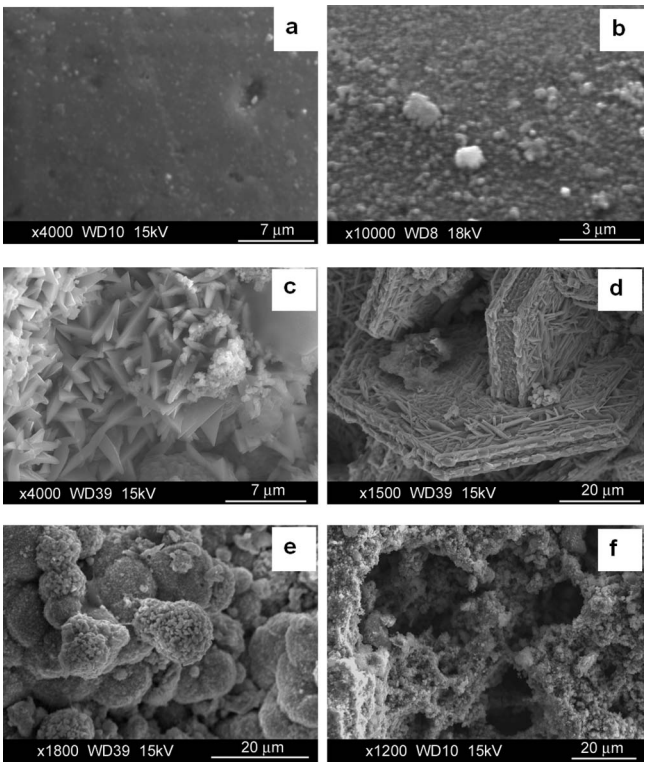

Fig. 1. Scanning electron microscopy (SEM) secondary electron images of: (a) uncoated glass bead (GB); (b) iron oxide-coated glass bead, and (c)–(f) four dominant morphologies found in CP: (c) tabular crystals with some rhombohedral forms evident; (d) hexagonal plates organized into various microstructures coated with needle shaped goethite-like crystals; (e) spherical (or globular) nodules; and (f) micro- or cryptocrystalline materials that may include amorphous compounds

materials or amorphous iron such as ferrihydrite (Cornell and Schwertmann 1996). SEM proved to be a useful tool for visualization and morphological comparison of the investigated natural and synthetic iron (hydr)oxides. CP appeared very rough, with a large density of macropores, while IOCB had much less variation in particle size, although SEM is not an ideal tool to elucidate roughness. CP clearly contained a large portion of crystalline material, while IOCB coating appeared as a thin scattering of spheres on the order of 100–500 nm in diameter. Although SEM was able to document the presence of several distinct crystal morphologies in the CP, such images alone cannot be used for mineral identification.

EDS elemental analysis results are shown in Table 1 for CP, IOCB, and GB. The CP results were similar to those reported by Sarin et al. (2001) for corrosion scales in old iron pipes from the Boston area. Additionally, the authors reported between 1 and 4 atom % (at. %) Al and between 1 and 11 at. % Si as well as sporadic findings (<at. %) of Ca, Cu, and Zn. In this study Ca, Al, Si, Na, and Mg were all present in less than 1 at. %. It is known that the aqueous composition and other factors impact the formation of crystals, which may explain some of the observed differences (Cornell and Schwertmann 1996; Rieke et al. 1995). Water quality data for the two systems were comparable, with the exception that the CP used in this study were from a system with higher mean sulfate levels (32.0 mg/L compared to 5.6 mg/L). The sulfate form of green rust was later suggested by XRD.

EDS of GB showed typical glass composition including a ma-

Table 1. EDS Elemental Composition of CP, IOCB, and GB

Sample	Replicates	Ca	Fe	Na	Mg	Al	Si	S
CP	8	—	92.3	—	—	—	—	7.7
IOCB	3	7.7	3.5	9.9	5.1	2.3	71.5	—
GB	1	8.7	—	9.2	6.0	1.9	74.3	—

Note: All values are in atom %. Reported values are normalized and values of less than 1% are reported in the text. Numbers of replicates analyzed are based on variability found in preliminary investigations.

jority of Si with small amounts of Na, Mg, Al, and Ca. EDS of IOCB showed a similar composition to GB, with the addition of a small amount of Fe, demonstrating that the 1–2 μm excitation depth under the electron beam most likely exceeded the thickness of the iron oxide coating which was determined to be approximately 118 nm thick based on our depth profiling analysis (see Depth Profiling of SIM ToF-SIMS/AFM section). Thus, the sampling depth of EDS can make it impractical for thin film characterization.

Rastering of the EDS beam (1 μm spot size) across the sample surfaces yielded elemental maps that exhibited little spatial variation in elemental composition for any of the samples. This could indicate a relatively well-distributed Fe coating or, more likely, that the EDS with its 1–2 μm excitation depth is primarily probing the homogeneous silicon substrate and not the thin iron (hydr)oxide film.

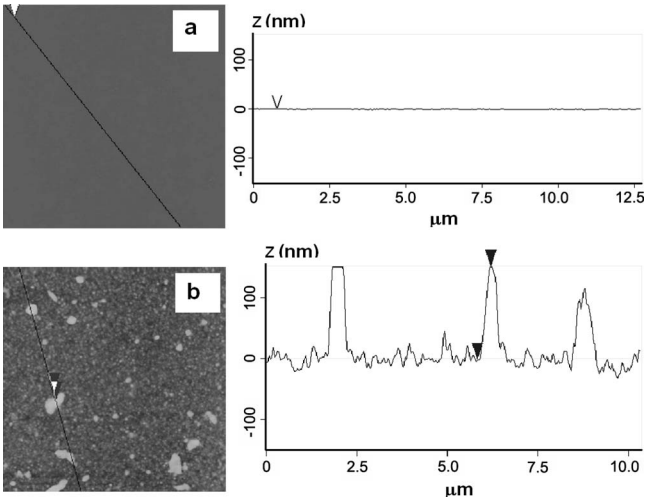

Fig. 2. Atomic force microscopy (height) images (10 μm × 10 μm) illustrating surface roughness: before (a); after coating of a cover slip (b) using AFM section analysis tool

AFM

Atomic force microscopy is suitable for quantifying roughness of relatively smooth and flat surfaces (e.g., thin films). Scans of various randomly selected regions on UC ($n > 45$) were obtained with good data agreement (i.e., similar roughness of the regions, see below); scans of randomly chosen areas on IOCC ($n > 150$) also resulted in good reproducibility. The AFM images and their corresponding cross sections shown are representative of the sample surfaces of an UC and an IOCC, respectively [Figs. 2(a and b)]. Comparisons of an UC [Fig. 2(a)] with an IOCC [Fig. 2(b)] show how the coating physically alters the relatively flat glass surface. The AFM image of an IOCC [Fig. 2(b)] and the SEM image of an IOCB [Fig. 1(b)] both suggest that the coating covered the surface with a scattering of micron and submicron domains. It is apparent, based on the section analysis, that the domains had a substantial range in height and diameter [Fig. 2(b)]. The surfaces of the GB and IOCB samples proved to be near the upper limit of our AFM capabilities with regard to vertical relief (~6 μm), and only a portion of the selected regions yielded good-quality scans (data not shown). Shellenberger and Logan (2002) presented AFM scans of glass beads, however it was not specified whether they were universally successful or if they were forced to find viewable areas by trial and error.

Additional capabilities of AFM include calculation of roughness parameters and estimation of the 3D surface area. These parameters are presented for UC and IOCC in Table 2. The root mean square (RMS) roughness is the standard deviation of the Z values (height measurements) within a given area, and mean roughness (Ra) represents the arithmetic average of deviations from the center plane (Instruments 1997). The iron coating increased the roughness over uncoated glass by a factor of approximately 27. Estimates of the 3D surface area from the AFM images show an increase of 6% after iron coating, which agrees well with the 6% increase estimated by BET for the coating of the GB. The IOCC were also analyzed in dry and fluid contact mode for comparison to the above-mentioned dry Tapping mode analysis with good data agreement (Table 2).

The AFM images contained a high level of detail and the image analysis software provided powerful analysis tools. Data

Table 2. Surface Area and Roughness of Glass Cover Slips before (UC) and after Iron Oxide Coating (IOCC)

Sample	n	AFM mode	2D area (μm^2)	3D area (μm^2)	RMS (nm)	Ra (nm)
UC	45	Dry TAP	100.00	100.03 ± 0.01	0.9 ± 0.2	0.6 ± 0.2
IOCC	45	Dry TAP	100.00	105.9 ± 0.9	27.3 ± 5.2	16.2 ± 3.1
IOCC	10	Dry contact	100.00	106.6 ± 0.7	24.3 ± 7.0	14.1 ± 2.8
IOCC	5	Fluid contact	100.00	105.9 ± 0.4	22.8 ± 4.2	13.2 ± 2.2

Note: IOCC were analyzed in three different AFM modes for comparison: dry tapping, dry contact, and fluid (in NanoPure water) contact. n=number of analyzed areas; root-mean square (RMS)=roughness; and Ra=average roughness.

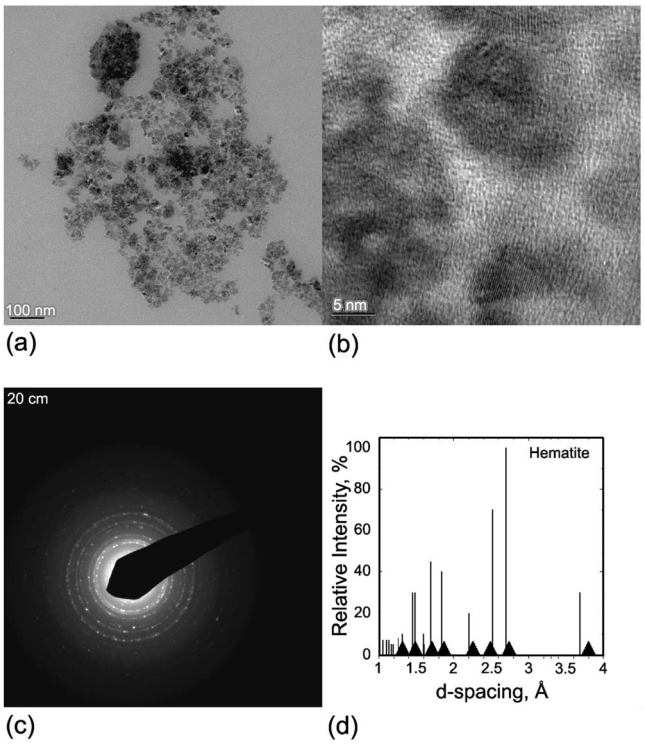

Fig. 3. Low resolution (a); high resolution TEM image (b) of synthetic iron oxide thin film removed from IOCB; (c) resulting electron diffraction pattern; bright spots indicate crystalline material while diffuse rings indicate poorly crystalline material; and (d) measured d spacing (Å) of electron diffraction pattern (triangles) compared with the standard pattern (lines) for hematite. Triangle width denotes average uncertainty.

such as those shown in Figs. 2(a and b) and Table 2 are of great value for comparison and for improved characterization of iron (hydr)oxide thin films. For methods to combine the strengths of SEM and AFM techniques in surface studies refer to Russel et al. (2003).

Depth Profiling by ToF-SIMS/AFM

Fourteen depth measurements of the coating on IOCC resulted in an average thickness of 124.6 ± 1.3 nm (mean $\pm 95\%$ confidence) including the Au layer. Subtracting the Au sputter coat of 6.4 nm as determined by analysis of a gold coated UC, the estimated thickness of the iron oxide coating formed by 9 h of forced thermal hydrolysis on a glass cover slip was approximately 118 nm. The combination of ToF-SIMS and AFM offered a powerful method to measure the depth of the iron (hydr)oxide coating with high surface sensitivity and spatial resolution. Alternative techniques for depth measurement of thin films include XPS and grazing-angle X-ray analysis (Kosaka et al. 1995).

TEM

In addition to SEM and AFM, TEM offered another method to visually inspect the Fe thin film and the CP [Figs. 3(a and b) and 4(a–c)]. TEM images of the coating revealed the occurrence of domains of approximately 5–50 nm, typically 10–20 nm in size [Fig. 3(b)]. Estimates obtained by using the AFM particle analysis tool showed that the majority of the domain sizes ranged

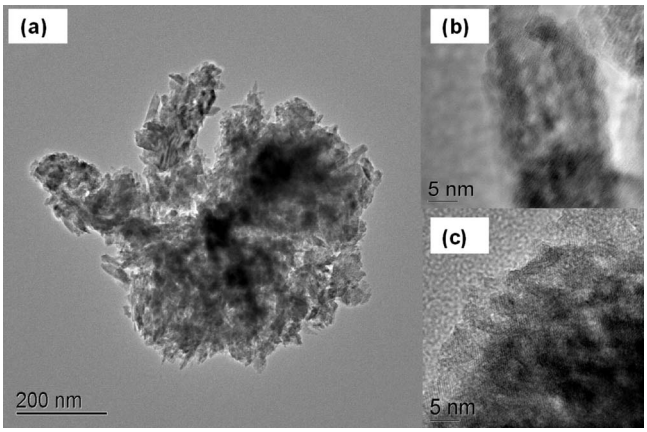

Fig. 4. TEM images of CP with: low resolution (a); and high resolution of selected areas (b)–(c). (b) and (c) show lattice fringing suggesting presence of α-FeOOH (b) and ferrihydrite ($Fe(OH)_3 \cdot (nH_2O)$) (c) based on calculations of d spacing from their respective electron diffraction patterns.

from 30 to 120 nm (data not shown). Some larger domains may have been destroyed in the process of abrading the coating for deposition on the carbon coated Cu grid. Previous studies showed domain sizes ranging from 10 to 70 nm using TEM on samples of synthetic iron (hydr)oxides, a result which is comparable to ours (Rieke et al. 1995). Lattice fringing in thicker particles was indicative of a crystalline thin film [Fig. 3(b)]. Elemental analyses of the coatings were similar to the results from SEM-EDS (data not shown).

The electron diffraction pattern [Fig. 3(c)] indicates crystalline and potential amorphous phases, however, the measured d spacing (Å) revealed the presence of hematite [Fig. 3(d)]. The presence of ferrihydrite was also suggested by the diffuse broad nature of the diffraction pattern at 1.49 Å [Fig. 3(c)]. Comparison of the sample diffraction data with standard data for maghemite, magnetite, lepidocrocite, and goethite suggests that these minerals are absent. This is in contrast to the results of Rieke et al. (1995) who used the same coating procedure but on a silicon wafer with a sulfonated self-assembled monolayer and found electron diffraction patterns consistent with goethite. However, a thermodynamic analysis by those authors showed that the expected products of this procedure might include ferrihydrite, goethite, and hematite, depending on the solution conditions and the precipitation sites.

TEM revealed that the CP consisted of a heterogenous mixture of iron (hydr)oxides [Fig. 4(a)]. Lattice fringing, d spacings based on SAED, and TEM images suggested for example the presence of goethite (α-FeOOH) [Fig. 4(b)] and ferrihydrite [Fig. 4(c)]. Resin embedded thin sections (70 nm thick) of the CP did not provide further information (data not shown).

FTIR and Mössbauer Spectroscopy

FTIR and Mössbauer spectroscopy were applied to analyze the IOCC. Only specular reflectance gave sufficient signal to distinguish the sample from the background, but the FTIR data (not shown) were inconclusive. Insufficient iron signal was also obtained using single samples by Mössbauer spectroscopy, thus multiple IOCC were stacked and analyzed together. The iron signal remained too weak for analysis with up to ten stacked IOCC, past which point the beam was so highly attenuated by the accu-

mulated thickness of the glass that a reliable signal could not be obtained (results not shown). The low signals obtained using FTIR and Mössbauer spectroscopy are most likely due to the limited thickness (118 nm) of the iron coating. CP were not analyzed by FTIR since it is not an appropriate technique for distinguishing complex mixtures of iron (hydr)oxides (Scheinost et al. 1998) or Mössbauer spectroscopy, because their composition were easily determined by XRD (as described in detail below). However, it should be pointed out that in contrast to XRD Mössbauer spectroscopy [and extended X-ray absorption fine structure (EXAFS) spectroscopy] can provide information about the presence of amorphous iron phases such as ferrihydrite although the interpretation of Mössbauer spectra can be quite challenging (Borch et al. 2007; Murad and Schwertmann 1980).

XPS

The Fe($2p3/2$) and O($1s$) core regions proved to be difficult to use for iron (hydr)oxide characterization since the binding energies for the iron (hydr)oxides are very similar. Even though the O($1s$) region of oxyhydroxides is unique due to the presence of two different oxygen binding energies (i.e., O_2^- and OH^-), care should be taken to prevent confusion between OH^- from physically adsorbed H_2O and FeOOH (McIntyre and Zetaruk 1977). Thus, the Fe $3p$ region from IOCC samples was studied and a spectral line value of 55.62 eV was measured. According to McIntyre and Zetaruk (1977), both hematite and maghemite possess Fe $3p$ spectral lines at 55.7 ± 0.15 eV, while goethite has its spectral line at 56.6 ± 0.2 eV. Both Fe($2p$) and Fe($3p$) spectra for the CP indicated the presence of Fe^{3+} (~712.0, 710.8, and 56.6 eV), Fe^{2+} (~708.0 and 54.0 eV), and Fe^0 metal (~706.6 and 53.0 eV) based on the peak broadening and consequently the need for more bands to fit the spectral peak envelopes (data not shown). The observed binding energies of the major core lines are in agreement with published values for α-FeOOH, Fe_3O_4, and Fe metal (McIntyre and Zetaruk 1977). However, to characterize the Fe mineralogy of CP by XPS is not a simple task and it should also be pointed out that XPS spectra only represent the surface mineralogy due to the very limited penetration depth of this technique. An elemental survey scan indicated the presence of sulfur and a minor contribution of calcium.

Powder and Grazing Incidence XRD

Powder XRD patterns of both intact and crushed IOCB and IOCC samples were negative for crystalline minerals, showing only the amorphous "hump" characteristic of silica glass. However, the presence of hematite as the sole crystalline phase was revealed by analyzing the thin film with a slow scan rate in grazing incidence mode [Fig. 5(a)]. Powder XRD analysis of CP showed a complex mixture of three and possibly four different iron (hydr)oxides: goethite (α-FeOOH orthorhombic), lepidocrocite (γ-FeOOH face-centered orthorhombic), magnetite (Fe_3O_4 isometric), likely green rust ($Fe_{3.6}Fe_{0.9}(O,OH,SO_4)_9$), and calcite ($CaCO_3$ trigonal) [Fig. 5(b)].

The presence of green rust has previously been reported in CP (AWWA et al. 1996; Refait et al. 2003). The weight percent of mineral phases can be semiquantitatively determined based on their reference intensity ratio (RIR); however, no RIR reference data exist for green rust. This prevents semiquantitative analysis of the other phases since one cannot ignore the contribution to the X-ray diffractogram from green rust. Nevertheless, a rough estimate of the weight percent indicated the relative abundance of the following phases: α-FeOOH $69 \pm 14\%$, Fe_3O_4 $18 \pm 4\%$, $6 \pm 1\%$ (γ-FeOOH), and $7 \pm 1\%$ $CaCO_3$ where the contribution of green rust was ignored. The observed iron (hydr)oxide minerals and their weight percents were in good agreement with results obtained previously from both iron and steel water pipes (Lin et al. 2001; Sarin et al. 2001).

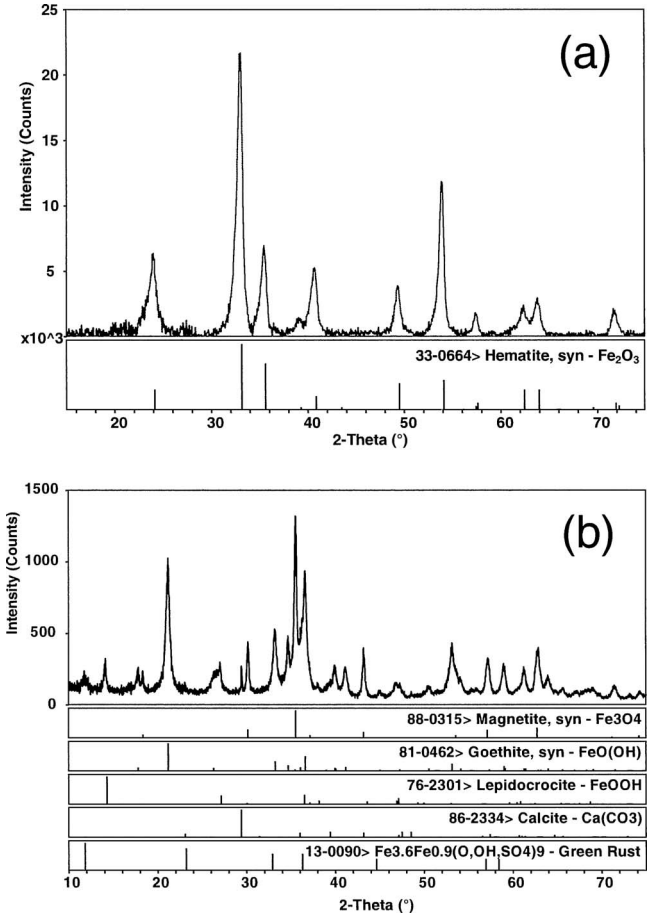

Fig. 5. (a) GI-XRD pattern of 118 nm thick synthetic iron oxide thin film (IOCC) after background subtraction of amorphous glass; (b) powder XRD pattern of CP compared to five most probable minerals based on database investigation

Conclusions

Surface Analytical Techniques and Their Relevance for Characterization of CP and IOCC

This study focused on the application of bulk and surface analytical techniques for the characterization of corrosion products and iron (hydr)oxide thin films. Table 3 summarizes the key results of these techniques and suggests their appropriate application towards either mineral identification or evaluation of physicochemical properties of iron (hydr)oxides.

The BET surface area and total iron content were simple to obtain and we found that the BET area ($0.068\ m^2/g$) and the Fe surface coverage ($7.4\ mg\ Fe/m^2$) of the IOCB were significantly smaller than for the CP ($26.2\ m^2/g$; $22.4\ mg\ Fe/m^2$). These results supported our previous findings that showed higher reactivity of CP than IOCB towards humic acid and disinfectants (Butterfield et al. 2002).

Table 3. Summary of Key Results That Each Technique Provided for Study of Iron Oxide Coated Glass Beads (IOCB) or Iron Oxide Coated Cover Slips (IOCC) and Corrosion Products (CP) from a Water Distribution System and Applicability of Each Technique

Result	Technique	IOCB/IOCC results	CP results	Applicability
Iron content	Fe by ferrozine method	7.4 mg Fe/m^2; IOCB	22.4 mg Fe/m^2	Widely applicable
Surface area	BET	0.068 m^2/g; IOCB	26.2 m^2/g	Widely applicable
High resolution (HR) images	SEM	Thin scattering of spheres 100–500 nm in diameter; IOCB	Rhombohedral, hexagonal plates, needle, globular and amorphous morphologies	Widely applicable
Elemental information	EDS	Ca, Fe, Na, Mg, Al, and Si; IOCB	Fe and S	Widely applicable
Precise morphology of smooth surfaces	AFM	Ra (nm) = 16.2 ± 3.1 and uniform coating thickness = 118 nm; IOCC	Too rough for analysis	Limited applicability and not easy to use
Identification of crystalline materials; semiquant, analysis	XRD	coating too thin for analysis; IOCC	Major phases: α-FeOOH, Fe_3O_4: minor phase: γ-FeOOH: probable phases: green rust and $CaCO_3$	Widely applicable
Identification of crystalline thin films	GID	α-Fe_2O_3; IOCC	Phases identified by XRD	Widely applicable
Oxidation state/binding energies	XPS	Probable phases: hematite or maghemite; IOCC	Probable phases: α-FeOOH, Fe_3O_4, and Fe metal	Limited applicability for mixtures of Fe (hydr)oxides
HR imaging; *d* spacing	TEM/SAED	Domain size 5–50 nm; phase ID of α-Fe_2O_3: IOCB	Mixture of iron (hydr)oxides (e.g., α-FeOOH)	Widely applicable but not easy to use
Spatial surface composition (m/z); depth profiling	ToF-SIMS	Depth profiling determined coating thickness in combination with AFM; IOCC	Not applicable	Applicable but not easy to use
Identification of mineral phases	FTIR and Mössbauer	Not applicable	See text	FTIR not applicable; Mössbauer applicable but not easy to use
Identification of crystalline and amorphous mineral phases	EXAFS[a]	Not applied in this study	Not applied in this study	Great technique but difficult to use and access
Identification of oxidation states	XANES[b]	Not applied in this study	Not applied in this study	Great technique but difficult to use and access

[a]EXAFS = extended X-ray absorption fine structure [for details on this technique see O'Day et al. (2004); Parsons et al. (2002)].

[b]XANES = X-ray absorption near edge structure [for details on this technique see O'Day et al. (2004); Parsons et al. (2002)].

XRD, XPS, EDS, and TEM-SAED were capable of identifying several crystalline phases, oxidation states, and the elemental composition of the corrosion products without extensive sample preparation. XRD proved to be the most useful technique for crystal phase identification of the CP and revealed the presence of goethite and magnetite as major phases and lepidocrocite as a minor phase.

These results are similar to those of Lin et al. (2001) and Sarin et al. (2001) who determined that their corrosion products consisted of goethite, magnetite, and lepidocrocite. In our study, the XRD analysis also suggested green rust [in agreement with the mineral morphology observed by SEM [Fig. 1(d)] and calcite as possible phases. The presence of green rust and calcite could be important since green rust is a very redox-active phase (O'Loughlin et al. 2003) and calcite is a good sorbent for many contaminants such as lead (Godelitsas et al. 2003). The presence of carbonates on Fe-oxides can also modify the activity of the oxide surfaces (Vikesland and Valentine 2002). The use of XPS and SAED for CP characterization is not a simple task based on the complexity of CP and therefore not recommended. The nanocrystalline hematite structure of the synthetic iron oxide thin film was revealed distinctively using GI-XRD and this result was partly supported by TEM-SAED, which identified hematite and potentially ferrihydrite, and XPS, which indicated the presence of hematite or maghemite. Consequently, it is recommended to use the grazing-incidence mode of XRD for phase identification of nanometer thin iron oxide coatings.

Mössbauer and FTIR spectroscopy were not capable of identifying the nature of the Fe (hydr)oxide thin film due to its limited thickness. FTIR is not recommended for identification of complex mixtures of Fe (hydr)oxides such as CP based on previous studies (Scheinost et al. 1998) and Mössbauer spectroscopy was not applied to the CP in this study.

Imaging techniques including AFM, SEM, and TEM were useful in providing gross comparisons of crystallinity, roughness, domain size, and surface area (Table 3). SEM may be used on a variety of samples (e.g., IOCB and CP) for bulk comparison, while AFM can provide detailed information such as roughness in the nanoscale range of relatively smooth coatings with a vertical relief of a few micrometers. TEM requires a thin sample made either by sectioning or by deposition of small particles onto a Cu grid. TEM proved to be a powerful tool for detailed imaging particularly in combination with SAED for phase identification and EDS for identification of the elemental composition. If the thickness of a very thin coating is of interest, it may be measured with high surface sensitivity and spatial resolution by the combined application of ToF-SIMS and AFM; this depth profiling technique revealed the presence of a 118 nm thick Fe coating on the glass cover slips.

In general, a combination of commonly available characterization techniques, such as SEM with EDS, TEM with SAED, XRD, and grazing incidence-XRD, would likely be most worthwhile.

These results illustrate the relative usefulness of several analytical tools that can be used to evaluate the chemistry and topography of corrosion products and their surrogates. Armed with this information, those interested in the composition of deposits and scales on iron distribution system surfaces and how they impact reactions associated with water quality changes can select the appropriate analytical methods.

Acknowledgments

Analytical work was performed at the Image and Chemical Analysis Laboratory at Montana State University (MSU) and the W. R. Wiley Environmental Molecular Sciences Laboratory (EMSL) at Pacific Northwest National Laboratory, operated for the Department of Energy by Battelle. Special thanks go to Alice Dohnalkova, Ravi Kukkadapu, and David McCready at EMSL for their scientific and technical contributions. Support was provided by Colorado State University to the lead writer, the U. S. Department of Defense, Army Research Office, Grant No. DAAD19-99-1-0092, the USEPA through its Office of Research and Development partially funded and collaborated in this research under Agreement No. CR-826927010, and this research was also partially supported by the U.S. Department of Energy, Office of Science, Environmental Management Science Program, under Grant No. DE-FG02-03ER63582. The writers also acknowledge the thoughtful comments provided by the associate editor and four anonymous reviewers.

References

American Water Works Association (AWWA). (1996). *Internal corrosion of water distribution systems*, 2nd Ed., AWWA Research Foundation, Denver.

American Water Works Association (AWWA). (2003). "Type of pipe material in place for water distribution." *AWWA MainStream*, Vol. 47, 1, American Water Works Association, Denver.

Appenzeller, B. M. R., Duval, Y. B., Thomas, F., and Block, J. (2002). "Influence of phosphate on bacterial adhesion onto oxyhydroxide in drinking water." *Environ. Sci. Technol.*, 36, 646–652.

Arce, F. T., Avci, R., Beech, I. B., Cooksey, K. E., and Wigglesworth-Cooksey, B. (2003). "Microelastic properties of minimally adhesive surfaces: A comparative study of RTV11TM and Intersleek elastomers™." *J. Chem. Phys.*, 119(3), 1671–1682.

Benjamin, M. M., Sletten, R. S., and Bailey, R. P. (1996). "Sorption and filtration of metals using iron-oxide-coated sand." *Water Res.*, 30, 2609–2620.

Borch, T., Masue, Y., Kukkadapu, R. K., and Fendorf, S. (2007). "Phosphate imposed limitations on biological reduction and alteration of ferrihydrite." *Environ. Sci. Technol.*, 41(1), 166–172.

Butterfield, P. W., Camper, A. K., Biederman, J. A., and Bargmeyer, A. M. (2002). "Minimizing biofilm in the presence of iron oxides and humic substances." *Water Res.*, 36, 3898–3910.

Chang, Y. J., Li, C. W., and Benjamin, M. M. (1997). "Iron oxide-coated media for NOM sorption and particulate filtration." *J. Am. Water Works Assoc.*, 89(5), 100–113.

Cheng, Z. Q., Van Geen, A., Jing, C. Y., Meng, X. G., Seddique, A., and Ahmed, K. M. (2004). "Performance of a household-level arsenic removal system during 4-month deployments in Bangladesh." *Environ. Sci. Technol.*, 38(12), 3442–3448.

Chun, C. L., Hozalski, R. M., and Arnold, T. A. (2005). "Degradation of drinking water disinfection byproducts by synthetic goethite and magnetite." *Environ. Sci. Technol.*, 39(21), 8525–8532.

Chun, C. L., Hozalski, R. M., and Arnold, W. A. (2007). "Degradation of disinfection byproducts by carbonate green rust." *Environ. Sci. Technol.*, 41(5), 1615–1621.

Cook, D. C. (2004). "Application of Mossbauer spectroscopy to the study of corrosion." *Hyperfine Interact.*, 153(1–4), 61–82.

Cornell, R. M., and Schwertmann, U. (1996). *The iron oxides*, VCH, New York.

Dong, H., Fredrickson, J. K., Kennedy, D. W., Zachara, J. M., Kukkadapu, R. K., and Onstott, T. C. (2000). "Mineral transformation associated with the microbial reduction of magnetite." *Chem. Geol.*, 169, 299–318.

Godelitsas, A., Astilleros, J. M., Hallam, K., Harissopoulos, S., and Putnis, A. (2003). "Interaction of calcium carbonates with lead in aqueous solutions." *Environ. Sci. Technol.*, 37(15), 3351–3360.

Hansen, B. O., Kwan, P., Benjamin, M. M., Li, C., and Korshin, G. V. (2001). "Use of iron oxide-coated sand to remove strontium from simulated Hanford tank wastes." *Environ. Sci. Technol.*, 35, 4905–4909.

Instruments, D. (1997). *DimensionTM 3100 instruction manual*, Santa Barbara, Calif.

Joshi, A., and Chaudhuri, M. (1996). "Removal of arsenic from ground water by iron oxide-coated sand." *J. Environ. Eng.*, 122, 769–771.

Kazi, Z. A. H., Kevin, C. B., and Christopher, M. M. (2006). "Iron oxide enhanced chlorine decay and disinfection by-product formation." *J. Environ. Eng.*, 132(12), 1609–1616.

Korshin, G. V., Benjamin, M. M., and Sletten, R. S. (1997). "Adsorption of natural organic matter (NOM) on iron oxide: Effects on NOM composition and formation of organo-halide compounds during chlorination." *Water Res.*, 31(7), 1643–1650.

Kosaka, T., Suzuki, S., Inoue, H., Saito, M., Waseda, Y., and Matsubara, E. (1995). "XPS/GIXS studies of thin oxide films formed on Fe-Cr alloys." *Appl. Surf. Sci.*, 103, 55–61.

Kukkadapu, R. K., Zachara, J. M., Fredrickson, J. K., and Kennedy, D. W. (2004). "Biotransformation of two-line silica-ferrihydrite by a dissimilatory Fe(III)-reducing bacterium: Formation of carbonate green rust in the presence of phosphate." *Geochim. Cosmochim. Acta*, 68(13), 2799–2814.

Lai, C. H., and Chen, C. Y. (2001). "Removal of metal ions and humic acid from water by iron-coated filter media." *Chemosphere*, 44(5), 1177–1184.

LeChevallier, M. W., Welch, N. J., and Smith, D. B. (1996). "Full scale studies of factors related to coliform regrowth in drinking water." *Appl. Environ. Microbiol.*, 62, 2201–2211.

Lin, J., Ellaway, M., and Adrien, R. (2001). "Study of corrosion material accumulated on the inner wall of steel water pipe." *Corros. Sci.*, 43(11), 2065–2081.

McIntyre, N. S., and Zetaruk, D. G. (1977). "X-ray photoelectron spectroscopic studies of iron oxides." *Anal. Chem.*, 49(11), 1521–1529.

McNeill, L. S., and Edwards, M. (2001). "Iron pipe corrosion in distribution systems." *J. Am. Water Works Assoc.*, 93(7), 88–100.

Murad, E., and Schwertmann, U. (1980). "The Mossbauer spectrum of ferrihydrite and its relations to those of other iron-oxides." *Am. Mineral.*, 65(9–10), 1044–1049.

National Research Council (NRC). (2006). *Drinking water distribution systems: Assessing and reducing risk*, National Academies Press, Washington, D.C.

O'Day, P. A., Rivera, N., Root, R., and Carroll, S. A. (2004). "X-ray absorption spectroscopic study of Fe reference compounds for the analysis of natural sediments." *Am. Mineral.*, 89(4), 572–585.

O'Loughlin, E. J., Kemner, K. M., and Burris, D. R. (2003). "Effects of Ag(I), Au(III), and Cu(II) on the reductive dechlorination of carbon tetrachloride by green rust." *Environ. Sci. Technol.*, 37(13), 2905–2912.

Parsons, J. G., Aldrich, M. V., and Gardea-Torresdey, J. L. (2002). "Environmental and biological applications of extended X-ray absorption fine structure (EXAFS) and X-ray absorption near edge structure (XANES) spectroscopies." *Appl. Spectrosc. Rev.*, 37(2), 187–222.

Perret, D., Gaillard, J., Dominik, J., and Atteia, O. (2000). "The diversity of natural hydrous iron oxides." *Environ. Sci. Technol.*, 34, 3540–3546.

Peulon, S., Legrand, L., Antony, H., and Chausse, A. (2003). "Electrochemical deposition of thin films of green rusts 1 and 2 on inert gold substrate." *Electrochem. Commun.*, 5(3), 208–213.

Refait, P., Memet, J.-B., Bon, C., Sabot, R., and Genin, J.-M. R. (2003). "Formation of the Fe(II)-Fe(III) hydroxysulphate green rust during marine corrosion of steel." *Corros. Sci.*, 45(4), 833–845.

Rieke, P. C., Marsh, B. D., Wood, L. L., Tarasevich, B. J., Liu, J., and Fryxell, G. E. (1995). "Aqueous solution deposition kinetics of iron oxyhydroxide on sulfonic acid terminated self-assembled monolayers." *Langmuir*, 11, 318–326.

Russel, P., Batchelor, D., and Thornton, J. (2003). "Scanning electron microscopy (SEM) and atomic force microscopy (AFM): Complementary techniques for high resolution surface investigations." ⟨www.di.com⟩, 1–12.

Sarin, P., Snoeyink, V. L., Bebee, J., Kriven, W. M., and Clement, J. A. (2001). "Physico-chemical characteristics of corrosion scales in old iron pipes." *Water Res.*, 35(12), 2961–2969.

Sarin, P., Snoeyink, V. L., Lytle, D. A., and Kriven, W. M. (2004). "Iron corrosion scales: Model for scale growth, iron release, and colored water formation." *J. Environ. Eng.*, 130(4), 364–373.

Scheidegger, A., Borkovec, M., and Sticher, H. (1993). "Coating of silica sand with goethite: Preparation and analytical identification." *Geoderma*, 58, 43–65.

Scheinost, A. C., Chavernas, A., Barron, V., and Torrent, J. (1998). "Use and limitations of second-derivative diffuse reflectance spectroscopy in the visible to near-infrared range to identify and quantify Fe oxide minerals in soils." *Clays Clay Miner.*, 46(5), 528–536.

Shellenberger, K., and Logan, B. E. (2002). "Effect of molecular scale roughness of glass beads on colloidal and bacterial deposition." *Environ. Sci. Technol.*, 36, 184–189.

Smith, S. E., Bisset, A., Colbourne, J. S., Holt, D., and Lloyd, B. J. (1997). "The occurrence and significance of particles and deposits in a drinking water distribution system." *J. N. Engl. Water Works Assoc.*, 111, 135–150.

Solozhenkin, P., Zouboulis, A., and Katsoyiannis, I. (2007). "Removal of arsenic compounds from waste water by chemisorption filtration." *Theor. Found. Chem. Eng.*, 41(5), 772–779.

Stenkamp, V. S., and Benjamin, M. M. (1994). "Effect of iron oxide coating on sand filtration." *New Sci.*, 83, 37–50.

Szabo, J. G., Rice, E. W., and Bishop, P. L. (2007). "Persistence and decontamination of *Bacillus atrophaeus subsp. globigii* spores on corroded iron in a model drinking water system." *Appl. Environ. Microbiol.*, 73(8), 2451–2457.

Thirunavukkarasu, O. S., Viraraghavan, T., and Subramanian, K. S. (2001). "Removal of arsenic in drinking water by iron oxide-coated sand and ferrihydrite-batch studies." *Water Qual. Res. J. Canada*, 36(1), 55–70.

Vertes, A., and Czakonagy, I. (1989). "Mossbauer-spectroscopy and its application to corrosion studies." *Electrochim. Acta*, 34(6), 721–758.

Vikesland, P. J., and Valentine, R. L. (2002). "Iron oxide surface-catalyzed oxidation of ferrous iron by monochloramine: Implications of oxide type and carbonate on reactivity." *Environ. Sci. Technol.*, 36(3), 512–519.

Williams, M. M., and Braun-Howland, E. B. (2003). "Growth of *escherichia coli* in model distribution system biofilms exposed to hypochlorous acid or monochloramine." *Appl. Environ. Microbiol.*, 69(9), 5463–5471.